Imaging mantle discontinuities using multiply-reflected P-to-S conversions

Stephen S. Gao *, Kelly H. Liu

Department of Geological Sciences and Engineering, Missouri University of Science and Technology, Rolla, MO 65409, USA

A B S T R A C T

Improving the reliability and accuracy in the determination of the depth to velocity discontinuities in the Earth's mantle is essential for a better understanding of mantle dynamics, as well as for addressing such fundamental questions as the origin of mantle plumes and fate of subducted slabs. Most existing techniques that utilize receiver function stacking, which is perhaps the most-commonly used method to image mantle discontinuities, suffer from strong trade-offs between the depth and velocity anomalies above the discontinuities. Here we propose and test a procedure that utilizes both the P-to-S converted phase (Pds) and the multiply reflected and converted phase (Ppds) at the discontinuities to simultaneously determine the depth of mantle discontinuities and velocity anomalies in the overlying layer. The procedure includes masking the strong PP arrivals prior to computing receiver functions, computing non-plane wave travel-times for Pds and Ppds for accurate moveout corrections, and utilizing the discrepancies in the apparent discontinuity depths from Pds and Ppds to simultaneously estimate velocity anomalies and discontinuity depths that are independent of velocity anomalies. Application of the procedure to data recorded by stations in seven radius = 1.5° circles along a 780 km N–S profile centered at the Yellowstone hotspot reveals lower-than-normal upper mantle and MTZ velocities beneath Yellowstone, a positive temperature anomaly of 40–190 °C in the vicinity of the 410 km discontinuity (d410), and a lower-than-normal temperature in the vicinity of the 660 km discontinuity (d660). The perceived hotspot is not associated with a localized depression of the d410 or an uplift of the d660, suggesting that the proposed mantle plume does not traverse the MTZ beneath the profile.

© 2013 Elsevier B.V. All rights reserved.

1. Introduction

The mantle transition zone (MTZ) is a layer with a global average thickness of about 241–243 km (Flanagan and Shearer, 1998; Gu et al., 1998; Shearer, 2000) bounded by the 410-km and 660-km discontinuities, which are generally believed to be phase transition boundaries in the peridotite mantle (Ringwood, 1975). Temperature, pressure, and water-content dependence of the onset of the phase transitions determines the depths of the discontinuities (Ohtani and Litasov, 2006). Consequently, accurate determination of the depths of the discontinuities and the associated thickness of the MTZ is essential for the understanding of mantle structure and dynamics.

One of the most-commonly used techniques to measure the depths of the discontinuities is stacking of source-normalized radial component seismograms (or receiver functions). The receiver function (RF) technique has been successfully applied to a variety of tectonic settings, such as perceived mantle plumes (Dueker and Sheehan, 1997; Shen et al., 1998; Fee and Dueker, 2004; Cornwell et al., 2011; Schmandt et al., 2012), continental extensional zones (Liu and Gao, 2006; Jasbinsek et al., 2010; Cao and Levander, 2010), subduction zones (Liu et al., 2003; Ai et al., 2005; Ozacar et al., 2008), stable continents (Li et al., 1998; Gao et al., 2002), and on the global scale (Shearer, 1991; Lawrence and Shearer, 2006; Andrews and Deuss, 2008).

A number of previous RF studies used either velocities in a standard Earth model such as the IASP91 (Kennett and Engdahl, 1991) or tomography-derived velocities with large uncertainties for moveout correction and time-to-depth conversion. Due to the intrinsic trade-off between the velocities above the discontinuities and the resulting depths, the resulting apparent discontinuity depths can be significantly different from the true depths. The trade-off is particularly problematic for determining the existence of mantle plumes in the MTZ (e.g., Shen et al., 1998; Foulger et al., 2001; Das-Sharma et al., 2010; Fee and Dueker, 2004; Cao and Levander, 2010; Schmandt et al., 2012), because while the higher-than-normal temperature associated with a mantle plume may lead to a thinned MTZ in an olivine-dominated system (Bina and Helffrich, 1994), the lower-than-normal velocities delay the travel-times of the P-to-S converted phases and result in an apparent thickening of the MTZ. These opposing effects of
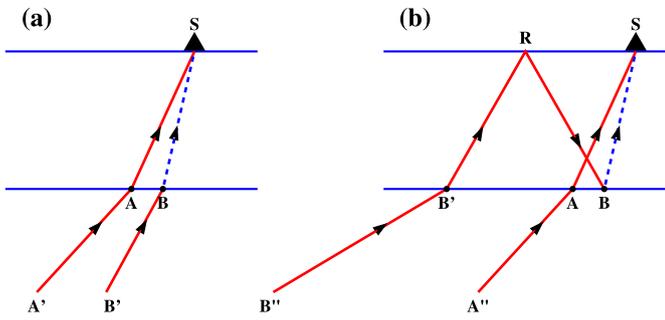
Fig. 1. Schematic diagrams showing the ray path of the direct P-wave (solid line segments) which pierces the discontinuity at point A, and that of the Pds (left plot) and Ppds (right plot). P-to-S conversion takes place at point B. Dashed line segments represent converted S-waves.

mantle plumes on the observed thickness of the MTZ contribute to the controversies regarding the depth extent of mantle plumes.

Here we present an approach to simultaneously estimate the velocity-independent depths ("true depths") of the MTZ discontinuities and the average P- and S-wave velocity anomalies in the overlying layer, by utilizing both P-to-S converted waves from the discontinuities and their multiples. The results can be used to infer anomalies in the temperature and water content in the MTZ (see Ohtani and Litasov, 2006 for a recent review of the effects of temperature and water on MTZ thickness) and be used as first-order constraints for tomographic inversions.

2. Strong presence of the Ppds phase

In this study we refer to the P-to-S converted phase from a discontinuity as Pds. In particular, we use P4s to refer the P-to-S conversion from the d410, and P6s for that from the d660. In addition to Pds, the procedure described below also uses the

Ppds phase, which is a P-wave traveling through a discontinuity, being reflected downward by the free surface of the Earth as a P-wave, and then reflected upward by the discontinuity as an S-wave (Fig. 1). Similar to the nomenclature for the direct converted phases, we use Pp4s and Pp6s to represent the Ppds phase associated with the d410 and d660, respectively. While Pds is composed of an S-leg, Ppds is composed of two P-legs and one S-leg (Fig. 1). Although it is not used in the procedure described below due to its weak amplitude, a phase composed of two S-legs and one P-leg is referred to as Psds, which has a negative polarity while Pds and Ppds have a positive polarity (relative to the polarity of the direct P-wave).

To evaluate the observability of the Ppds (and perhaps the Psds) phases associated with the MTZ discontinuities, we requested broadband seismic data recorded by all the stations in a radius = 6° circle centered at (−97°E, 42°N) on the central Great Plains of North America (Fig. 2), from the IRIS (Incorporated Research Institutions for Seismology) DMC (Data Management Center). The data were recorded in the time period between mid-1992 and early 2013. The epicentral distance range of the events is between 40° and 100°, and the cutoff magnitude is calculated using $M_c = 5.2 + (D_e - 30.0)/(180.0 - 30.0) - H_f/700$, where D_e is the epicentral distance in degree, and H_f is the focal depth in km (Liu and Gao, 2010).

The 3-component seismograms are filtered in the frequency band of 0.02–0.2 Hz using a 4-pole, 2-pass Bessel filter, and are converted into radial RFs using the procedure of Ammon (1991). Before the computation of the RFs, we apply a pair of exponential weighting functions with a half width of 30 s and centered at the theoretical arrival time of the PP-phase (t_{pp}) to reduce the amplitude of the PP phase on the vertical, N–S, and E–W components. This step is necessary for reducing the degenerating effect to the resulting RFs by the PP arrivals which have very different ray parameters than the P-waves. The functions are defined as
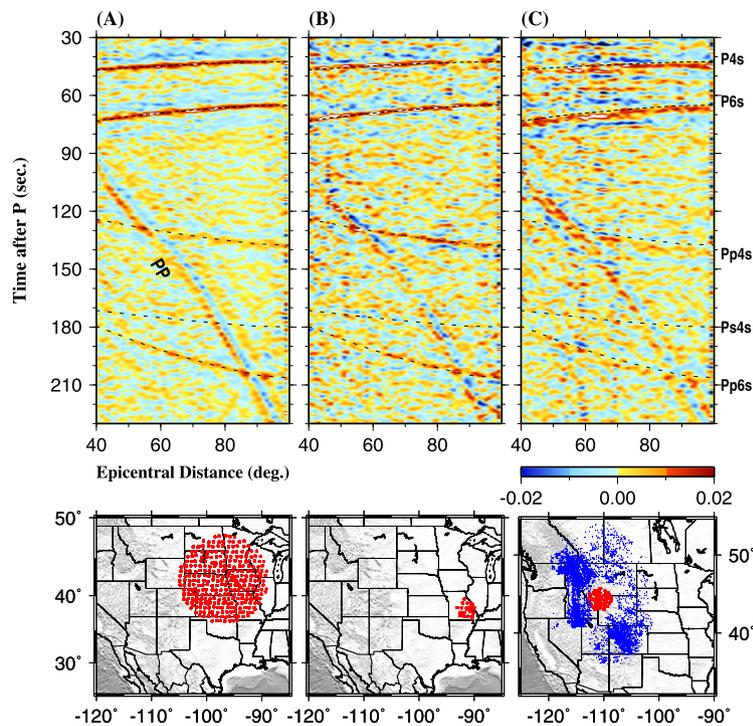
Fig. 2. (Top panels): Radial receiver functions stacked in epicentral distance bins. (A) Results using stations in a radius = 6° circle on the Great Plains of North America; (B) Results using stations from a radius = 1.5° circle in eastern Missouri; (C) Results using stations from a radius = 1.5° circle centered at the Yellowstone hotspot. (Bottom panels): Distribution of seismic stations (circles) used to produce the binned RFs shown in the panel above. Blue dots in the lower-right figure represent Ppds ray-piercing points at 530 km depth.

$$G(t) = \begin{cases} e^{-0.2(t-t_{pp}+30.0)} & \text{if } t_{pp} - 30.0 \text{ s} < t < t_{pp} - 5.0 \text{ s}; \\ 0 & \text{if } t_{pp} - 5.0 \text{ s} < t < t_{pp} + 5.0 \text{ s}; \quad (1) \\ e^{-0.2(-t+t_{pp}+30.0)} & \text{if } t_{pp} + 5.0 \text{ s} < t < t_{pp} + 30.0 \text{ s}. \end{cases}$$

Manual screening of the RFs results in a total of 24,640 high-quality RFs from 199 USArray Transportable Array and 23 other stations. The RFs are grouped into 2° focal-depth corrected epicentral distance bins with 1° overlap between neighboring bins, and those in the same bins are averaged. The results (Fig. 2A) show that in addition to the commonly-observed P-to-S conversions from the d410 and d660, the Ppds arrivals from the d410 and d660 are clearly observed in the time range of 120 s to 140 s and 170 s to 210 s, respectively. The negative Ps4s and Ps6s phases are barely observed, suggesting that they have a much smaller amplitude than the corresponding Ppds phases, probably due to the stronger attenuation of the S-waves relative to that of the P-waves as demonstrated by synthetic studies (e.g., Clarke and Silver, 1991; Liu, 2003). Note that there is a trade-off between the amount of remaining PP energy and the energy of the Ppds phases on the resulting RFs (Fig. 2). The parameters used in Eq. (1) reduced the PP energy to a level that is lower than that of the Pds phases from the MTZ discontinuities, and maximized the epicentral distance range in which the Ppds phases can be used. Schaeffer and Bostock (2010) used the P4s and Pp4s phases and their precursory arrivals to image a low velocity layer atop the d410 beneath northwestern Canada. In contrast to the procedure used in this study, they used only the section of the RFs prior to the PP phase which limited the usable epicentral distance range to about 70°–100° for Pp4s, and 95°–100° for Pp6s (Fig. 2).

For surface events, a number of reverberations on the source side can produce arrivals that have exactly the same arrival time as that of Ppds. An example of such reverberations is an arrival from a surface event located at point S in Fig. 1b, consisting of an S-wave leg (SB), two short P-wave legs (BR and RB′), and one long P-leg (from B′ to the receiver). Fortunately, for these source-side reverberations, the final leg (i.e., the long P-leg) of the ray path that reaches the receiver is a P-wave, which, due to the steep angle of incidence, has a negligible amplitude on the radial component relative to the P-to-S converted wave from the receiver side. In addition, when events with the full range of focal depths are used, the arrivals are not stacked coherently and thus further reduces the effects of the source-side reverberations on the stacked RFs. Thus the observed Ppds arrivals on the stacked RFs (Fig. 2) mostly represent receiver-side conversions.

To test the RF stacking procedure, which is described in the next section, we also obtained and processed seismograms from stations within $R = 1.5°$ circles centered at the Yellowstone hotspot (Fig. 2C) and at Global Seismic Network (GSN) station CCM (Cathedral Cave, Missouri; longitude: 91.245°W, latitude: 38.056°N) on the Great Plains (Fig. 2B). The number of high-quality RFs for Yellowstone is 7469, and that for CCM is 2816. Although the Pp4s and Pp6s phases in the smaller circles are less strong than those in the $R = 6°$ circles due to the reduced number of RFs participated in the stacking, their presence is still clearly observed (Fig. 2). The MTZ arrivals are enhanced when the RFs are moveout corrected and stacked, as described below.

3. Moveout correction and stacking of Pds and Ppds arrivals

The vast majority of previous studies performed RF stacking and time-to-depth conversion using the plane-wave assumption, in which the ray-parameters for the direct P-wave and the converted S-wave are considered as the same (Sheriff and Geldart, 1993; Gurrola et al., 1994; Dueker and Sheehan, 1997; Liu et al., 2003). The magnitude of the error caused by this assumption is greater for deeper discontinuities (Lawrence and Shearer, 2006). In addition, because larger ray-parameters (i.e., rays from closer events)

correspond to greater biases under the plane wave assumption, artificial spatial variations of the depth to the discontinuities could arise from the varying epicentral distances from the world's major seismic zones. The plane-wave assumption leads to distance-dependent errors with magnitude as large as 2.5 s for the Ppds phases in the epicentral distance range of 40°–60°. The mismatch is small for Pds, with a maximum value of about 0.4 s for P6s in the above distance range (see electronic supplement).

The resulting non-plane wave travel-times for Pds and Ppds, $T^{(Pds)}$ and $T^{(Ppds)}$, are then used separately to moveout correct and stack RFs recorded in a given area, i.e.,

$$S^{(Pds)}(d) = \frac{1}{N} \sum_{i=1}^{N} S_i[T_i^{(Pds)}], \quad (2)$$

$$S^{(Ppds)}(d) = \frac{1}{N} \sum_{i=1}^{N} S_i[T_i^{(Ppds)}], \quad (3)$$

where $S^{(Pds)}(d)$ is the stacking amplitude for a candidate discontinuity at depth d obtained using the Pds travel-times, N is the number of RFs, $T_i^{(Pds)}$ and $T_i^{(Ppds)}$ are the Pds and Ppds moveout times, respectively, of the ith receiver function at depth d, and $S_i(T_i)$ is the amplitude of the ith receiver function at time T_i.

Fig. 3 shows resulting depth curves of the above moveout correction and stacking procedure, using RFs shown in Fig. 2. Relative to the arrivals on the curves created by the Pds phase, the arrivals associated with the MTZ discontinuities are sharper on the curves produced by the Ppds phase. This is caused by the fact that relative to the Pds, the Ppds phase has two additional P-wave legs in the layer above the discontinuity (Fig. 1). Consequently, the same amount of change of discontinuity depth leads to greater travel-time changes for Ppds, resulting in higher vertical resolution. The resulting depths of the discontinuities from Pds and Ppds differ by as much as 9 km (for d660 beneath Yellowstone). As discussed in the next section, such discrepancies imply the existence of velocity anomalies above the discontinuities, and can be used to estimate the magnitude of the anomalies and the true depth of the discontinuities. Note that because the moveout correction is performed using velocities in the IASP91 standard Earth model, the depths to the d410 and d660 shown in Fig. 3 are apparent depths.

4. Determination of the true discontinuity depths and velocity anomalies above a discontinuity using apparent depths

After the moveout corrections, the arrival times and the corresponding discontinuity depths can be related using depth–time–velocity relations for vertically incident waves. Under the assumption of a constant velocity structure beneath the area sampled by the Pds and Ppds phases, the arrival time difference between the converted S-wave and the direct P-wave can be expressed as

$$T_{s-p}^{(Pds)} = H_T/(V_{s0} + \delta V_s) - H_T/(V_{p0} + \delta V_p), \quad (4)$$

and that for Ppds is

$$T_{s-p}^{(Ppds)} = H_T/(V_{s0} + \delta V_s) + H_T/(V_{p0} + \delta V_p). \quad (5)$$

where H_T is the true depth of the discontinuity, V_{p0} and V_{s0} are the mean P- and S-wave velocities, respectively, in the IASP91 standard Earth model above the discontinuity, and δV_p and δV_s are the P- and S-wave velocity anomalies, respectively.

The use of the velocities in the standard Earth model leads to an apparent depth of H_A, and the corresponding travel-times are the same as those in Eqs. (4) and (5) and can be expressed as

$$T_{s-p}^{(Pds)} = H_A^{(Pds)}/V_{s0} - H_A^{(Pds)}/V_{p0}, \quad (6)$$
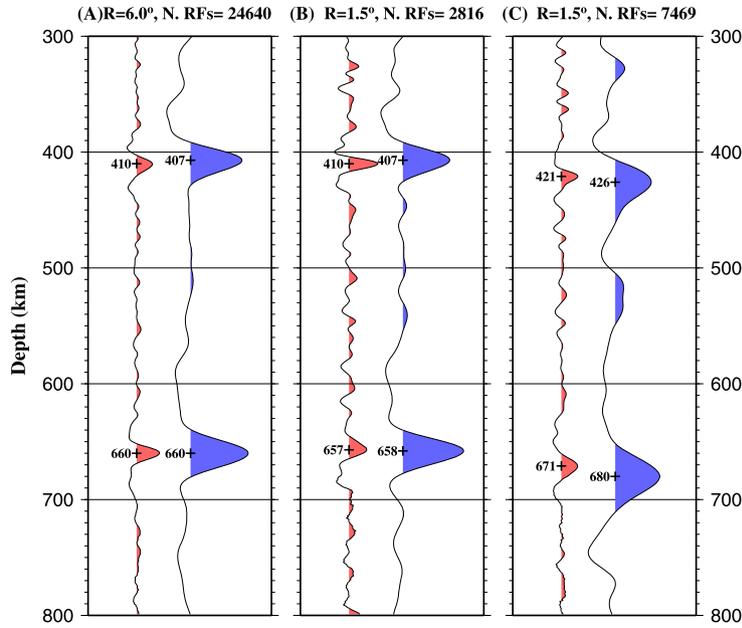
Fig. 3. Results of stacking of moveout-corrected RFs using Ppds (the curve on the left in each of the panels) and Pds (the curve on the right) for (A) Area A, (B) Area B, and (C) Area C in the previous figure. The numbers on the left of the peaks indicate their apparent depths.

and

$$T_{s-p}^{(Ppds)} = H_A^{(Ppds)}/V_{s0} + H_A^{(Ppds)}/V_{p0}. \tag{7}$$

Equating Eqs. (4) and (6), we get

$$H_A^{(Pds)} = \frac{V_{p0} + \delta V_p - V_{s0} - \delta V_s}{(V_{s0} + \delta V_s) \times (V_{p0} + \delta V_p)} \times \frac{V_{p0} \times V_{s0}}{V_{p0} - V_{s0}} H_T, \tag{8}$$

and from Eqs. (5) and (7), we have

$$H_A^{(Ppds)} = \frac{V_{p0} + \delta V_p + V_{s0} + \delta V_s}{(V_{s0} + \delta V_s) \times (V_{p0} + \delta V_p)} \times \frac{V_{p0} \times V_{s0}}{V_{p0} + V_{s0}} H_T. \tag{9}$$

Taking the ratio of the last two equations results in

$$\frac{H_A^{(Pds)}}{H_A^{(Ppds)}} = \frac{\alpha + \delta V_p - \delta V_s}{\beta + \delta V_p + \delta V_s} \times \frac{\beta}{\alpha}, \tag{10}$$

where $\alpha = V_{p0} - V_{s0}$, and $\beta = V_{p0} + V_{s0}$.

Eq. (10) indicates that $H_A^{(Pds)} = H_A^{(Ppds)} = H_T$ when the real velocities are the same as those in the standard Earth model (i.e., $\delta V_p = \delta V_s = 0$). The apparent depths obtained from Pds and Ppds are different when the real velocities are different from those in the standard Earth model. Thus the discrepancies between the apparent depths using Pds and Ppds are diagnostic of velocity anomalies above the discontinuities.
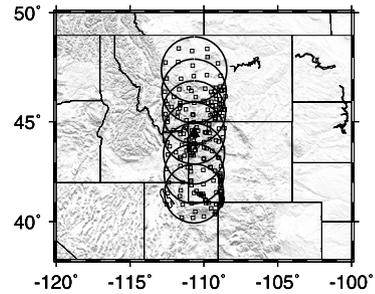
Under the assumption that the fractional P- and S-wave velocity anomalies are proportional, i.e.,

$$\frac{\delta V_s}{V_{s0}} = \gamma \frac{\delta V_p}{V_{p0}}, \tag{11}$$

where γ is a constant, we can solve for δV_p using Eqs. (10) and (11), i.e.,

$$\delta V_p = \left(\alpha \times \beta \times \left(H_A^{(Ppds)} - H_A^{(Pds)} \right) \right)$$
$$\times \left(\alpha \times (1 + \gamma V_{s0}/V_{p0}) \times H_A^{(Pds)} \right.$$
$$\left. - \beta \times (1 - \gamma V_{s0}/V_{p0}) \times H_A^{(Ppds)} \right)^{-1}. \tag{12}$$

Once δV_p and δV_s are determined using Eqs. (12) and (11), respectively, the true depth of the discontinuity, H_T, can then be found using Eqs. (8) or (9).


Fig. 4. Seismic stations (squares) in 7 radius = 1.5° circles along the −110.67° longitudinal line centered at Yellowstone (triangle). The center of the circles has a latitude of $i + 40.43°$ where $i = 1°$ for the southernmost circle, ... and $i = 7°$ for the northernmost circle.

From the resulting true depths of the d410 ($H_T^{(4)}$) and d660 ($H_T^{(6)}$) and the mean velocities above them ($V_p^{(4)}$, $V_p^{(6)}$, $V_s^{(4)}$, and $V_s^{(6)}$), the velocity anomalies of the MTZ ($\delta V_p^{(M)}$ and $\delta V_s^{(M)}$) can be found using Eq. (11) and the following partitioning relationship of the S- and P-wave differential times, i.e.,

$$\frac{H_T^{(6)}}{V_s^{(6)}} - \frac{H_T^{(6)}}{V_p^{(6)}} - \frac{H_T^{(4)}}{V_s^{(4)}} + \frac{H_T^{(4)}}{V_p^{(4)}}$$
$$= \frac{H_T^{(6)} - H_T^{(4)}}{V_{s0}^{(M)} + \delta V_s^{(M)}} - \frac{H_T^{(6)} - H_T^{(4)}}{V_{p0}^{(M)} + \delta V_p^{(M)}}, \tag{13}$$

where $V_{p0}^{(M)}$ and $V_{s0}^{(M)}$ are the mean MTZ velocities in the standard Earth model. Obviously, the accuracy of the resulting MTZ velocity anomalies is dependent on that of the true depths and that of the velocity anomalies above the d410 and d660.

We next apply the above formulas to the apparent MTZ discontinuity depths (Fig. 3) in three areas (Fig. 2), by assuming a γ value of 2.0 which is representative for most continental areas (Schmandt and Humphreys, 2010). The effects of the γ value on the resulting parameters are discussed in the next section. Here we refer to the $R = 6°$ area in the Great Plains as Area A, the $R = 1.5°$ area centered at station CCM as Area B, and the $R = 1.5°$ area centered at the Yellowstone hotspot as Area C.
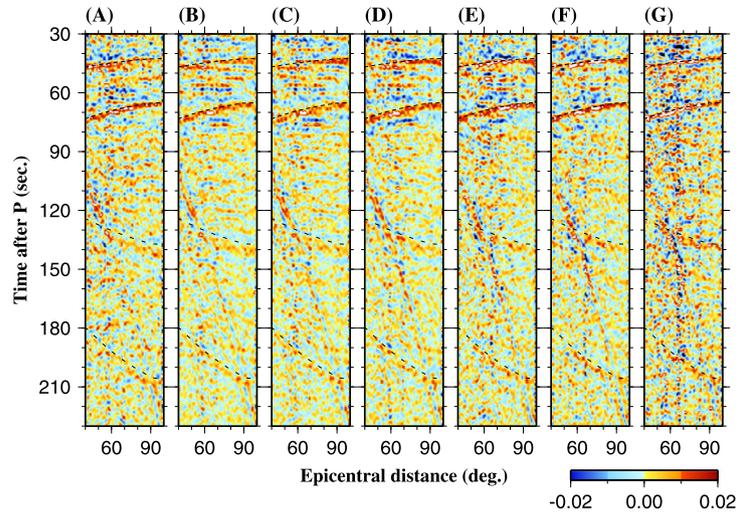
Fig. 5. Radial receiver functions stacked in epicentral distance bins recorded by stations in the 7 circles shown in the previous figure. Plot (A) is for the southern-most circle etc.

Based on Eqs. (12), (11), and (8), the 3 km depression of the apparent depths from Pp4s relative to P4s for Area A (Fig. 3) results in a true d410 depth of 413 km, a P-wave velocity anomaly of 0.46% (and an S-wave anomaly of twice as large) above the d410. The identical apparent depths of 660 km for the d660 from Pds and Ppds suggest that the true depth of the d660 is 660 km, and the average velocities above the d660 are identical with those in the IASP91 standard Earth model. Because the upper mantle has higher-than-normal velocities, this suggests that the MTZ has lower-than-normal velocities. Using Eq. (13), a P-wave anomaly of −0.69% is found for the MTZ. The MTZ thickness beneath Area A is 246 km which is slightly thicker than the global average (Shearer, 2000). For Area B, the resulting true depth is 413 and 656 km, respectively, for the d410 and d660, leading to a MTZ thickness of 243 km. The P-wave velocity anomaly above the d410 and the d660 and in the MTZ is 0.46%, −0.10%, and −0.92%, respectively. The results for Areas A and B suggest that while the upper mantle beneath the stable part of the North American craton has higher-than-normal velocities, the MTZ has normal temperature and slightly lower-than-normal velocities. For Area C, the resulting true depth of the d410 is 416 km, and that for the d660 is 662 km, leading to a MTZ thickness of 246 km. The upper mantle P-wave velocity anomaly is −0.74% and the MTZ anomaly is −0.80%. The MTZ thickness suggests a normal or even slightly colder-than-normal MTZ beneath this area.

5. Application to Yellowstone

We next apply the procedure to study spatial variations of the MTZ discontinuities in the vicinity of the Yellowstone hotspot (latitude 44.43°, longitude −110.67°) to further test the procedure. Broadband seismic data recorded by all the stations from mid-1992 to early 2013 in the area of 105°W to 115°W and 39°N to 50°N are requested from the IRIS DMC. The stations are then grouped into seven circles along the −110.67° longitudinal line with a radius of 1.5° (Fig. 4). The latitude of the center of the ith circle (where $i = 1, 2, \ldots 7$) is $i + 40.43°$ (so that the 4th circle is centered at the Yellowstone hotspot). For the sake of simplicity, in the following we refer to the area sampled by the first (south-most) circle as Y1, and that by the second circle as Y2 etc. The Pds and Ppds phases associated with the MTZ discontinuities are clearly observed on the binned RFs for all the 7 areas (Fig. 5). The number of RFs in the circles ranges from 2641 to 8175. The RFs recorded by the stations in each of the circles are then moveout corrected and stacked using Eqs. (2) and (3) for Pds and Ppds, respectively,
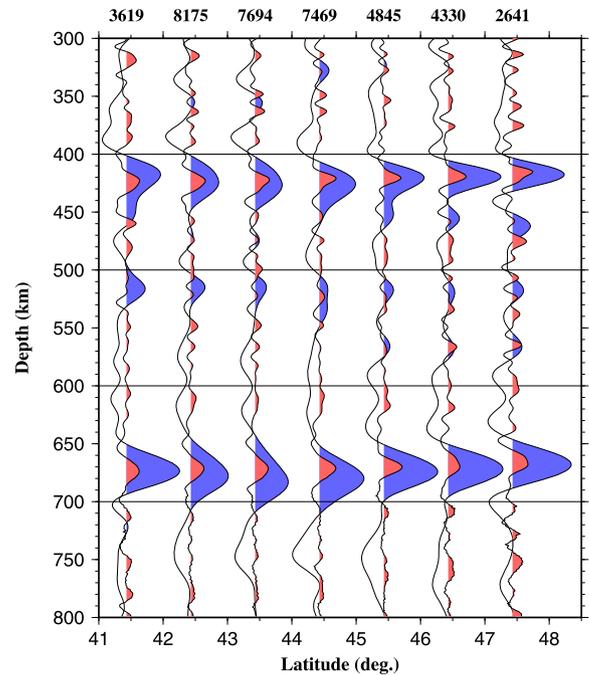
Fig. 6. Results of stacking of moveout-corrected RFs using Ppds (red curves) and Pds (blue curves) for the 7 groups of RFs shown in the previous figure. The number of RFs participated in the stacking is shown at the top of the traces. (For interpretation of the references to color in this figure legend, the reader is referred to the web version of this article.)

and the Pds and Ppds arrivals from the MTZ discontinuities are observed with a high signal to noise ratio in the resulting depth series (Fig. 6).

A 10-fold bootstrap resampling procedure (Efron and Tibshirani, 1986; Liu et al., 2003) was used to obtain the mean and standard deviation of the resulting apparent depths of the MTZ discontinuities and the velocity anomalies (Fig. 7). The apparent d410 depths determined from P4s and those from Pp4s are statistically identical for areas Y1, Y2, Y5, Y6, and Y7 (Fig. 7A), suggesting that the average velocity anomalies above the d410 are nearly zero, and that the true d410 depths are the same as the apparent depths. The depths obtained from P4s are significantly deeper than those from Pp4s for areas Y3 and Y4 (which is centered at Yellowstone), implying lower-than-normal upper mantle velocities beneath these
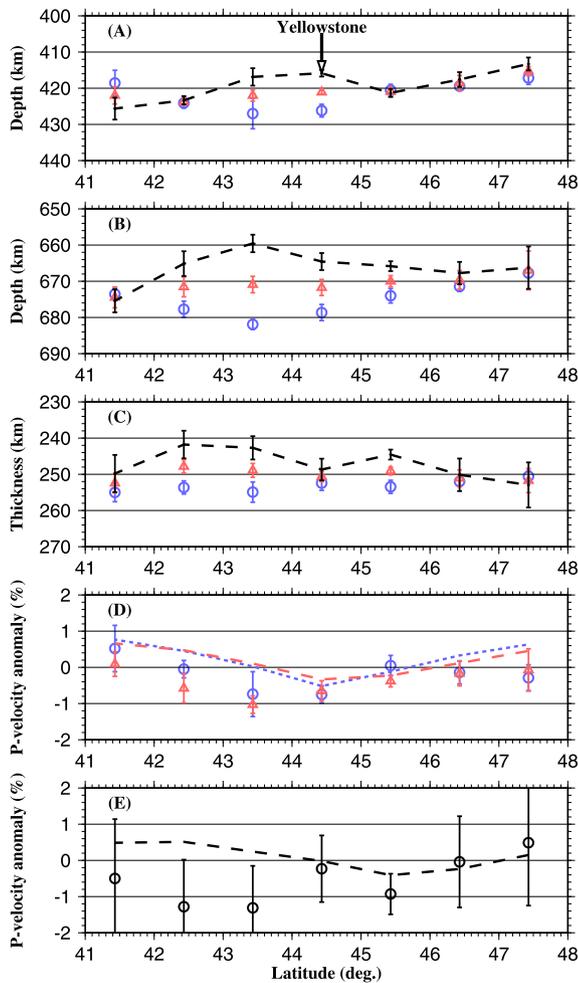
Fig. 7. Mean measurements obtained from bootstrap-stacking of RFs shown in Fig. 5. (A) Apparent depths for the d410 using the Pds (circles) and Ppds (triangles) phases. The dashed line shows the resulting true depth of the d410. (B) Same as (A) but for the d660. (C) Same as (A) but for the thickness of the MTZ. (D) P-wave velocity anomalies above the d410 (circles) and d660 (triangles). The short-dashed line and the long-dashed line show the average P-wave velocity anomalies above 420 km and 660 km, respectively, converted from the S-wave velocities of Obrebski et al. (2011), using a γ value of 2.0. (E) P-wave velocity anomalies in the MTZ (circles). The dashed line shows average MTZ P-wave velocity anomalies (Obrebski et al., 2011). The error bars represent two standard deviations.

areas. The true d410 depths computed using the apparent depths range from 413 to 426 km, indicating a temperature anomaly of 40–190 °C when a Clapeyron slope of 2.9 MPa/K is used (Bina and Helffrich, 1994) in the vicinity of the d410. The Yellowstone hotspot is not associated with a depression of the true d410 depth (Fig. 7A).

For the d660, the apparent depths determined from P6s are greater than those from Pp6s for areas Y2–Y5, suggesting negative velocity anomalies above the d660 beneath these areas (Fig. 7B). The resulting true d660 depths range from 660 to 675 km which are mostly greater than the global average (Shearer, 2000), indicating that the temperature in the vicinity of the d660 is lower than normal beneath the areas sampled by the stations. The MTZ thickness beneath the study area is between 242 km and 253 km with an average of 247 ± 4 km (Fig. 7C), which is slighter thicker than the global average of 243 km (Flanagan and Shearer, 1998).

The resulting mean velocity anomalies above the discontinuities are comparable with those obtained from a joint inversion of body- and surface-wave tomography (Obrebski et al., 2011) at most of the areas, especially when the uncertainties in the tomography results are considered. Similarly, the MTZ velocity anomalies deter-

mined using Eq. (13) have large uncertainties and are statistically consistent with the results of seismic tomography at most of the areas (Fig. 7E).

In summary, results obtained using Pds and Ppds suggest that while the proposed Yellowstone hotspot is associated with an upper mantle low-velocity anomaly, the anticipated depression of the d410 or the uplift of the d660 associated with a well-defined mantle plume beneath Yellowstone is not observed, suggesting that the source of magma may reside in the upper mantle. This conclusion is consistent with that from some previous studies (Leeman et al., 2009; Cao and Levander, 2010) but are different from other studies (e.g., Fee and Dueker, 2004; Schmandt et al., 2012). The contrasting conclusions, which were mostly caused by the differences in the data, techniques, and assumptions employed by the numerous studies, call for additional investigations of the nature of the hotspot (Fouch, 2012). Our results, however, do not exclude the possibility that the mantle plume enters the MTZ from outside the area sampled by the majority of the seismic ray paths. More detailed discussions and comparison of results from previous studies and those obtained using the technique proposed in this study will be presented in a followup report for the entire western and central United States (Gao and Liu, in preparation).

6. Discussion

6.1. Influence of γ

The γ value defined in Eq. (11) is a function of temperature, rock composition, and degree of partial melting (Karato, 1993). This value is found to be in the range of 1.5–2.5 for most continental areas (Schmandt and Humphreys, 2010). A γ value of 2.0 is used to obtain the velocity anomalies and MTZ discontinuity depths. To estimate the magnitude of errors in the results when γ beneath a given area is different from 2.0, we computed velocity anomalies and discontinuity depths for a series of γ values ranging from 1.5 to 4.0 for Area C (Figs. 2 and 3). The results (Fig. 8) suggest that a larger γ value results in greater depths and higher velocity anomalies. However, the resulting MTZ thickness is only weakly dependent on the γ values, with a peak-to-peak magnitude of less than 3 km, and the resulting P-wave velocity anomalies have a peak-to-peak magnitude of about 1%.

6.2. Effects of lateral variations of discontinuity depth and velocities

The above procedure assumes that in the area sampled by the direct P, Pds, and Ppds phases (Fig. 1), the discontinuity has a constant depth and laterally invariant velocities. Because the seismic rays travel through or reflect at the discontinuity at different locations (Fig. 1), undulations of the depth and lateral variation of the velocities lead to biased results. For instance, for Pds (Fig. 1a), if point A is deeper than point B, the resulting apparent depth will be shallower than the case when point A is at the same depth as point B, due to a smaller S-P arrival time difference associated with the longer ray path from A to S (Fig. 1a). The behavior of the Ppds phase is more complicated because it interacts with the discontinuity twice at points B and B' (Fig. 1b). A tilting interface that dips toward the left will increase the travel-times of both the direct P and the Ppds phases.

The size of the volume sampled by the phases increases with increased depth of the discontinuity and the ray parameter of the incident ray path. For a direct P-wave ray parameter of 6.15 s/degree (for a surface event with an epicentral distance of 70°), the angular distance from the station is about 1.0° for point A, 2.0° for point B, and 5.1° for point B' (Fig. 1b) at the depth of 410 km. These values increase to 1.9°, 3.8°, and 9.5° at 660 km depth.
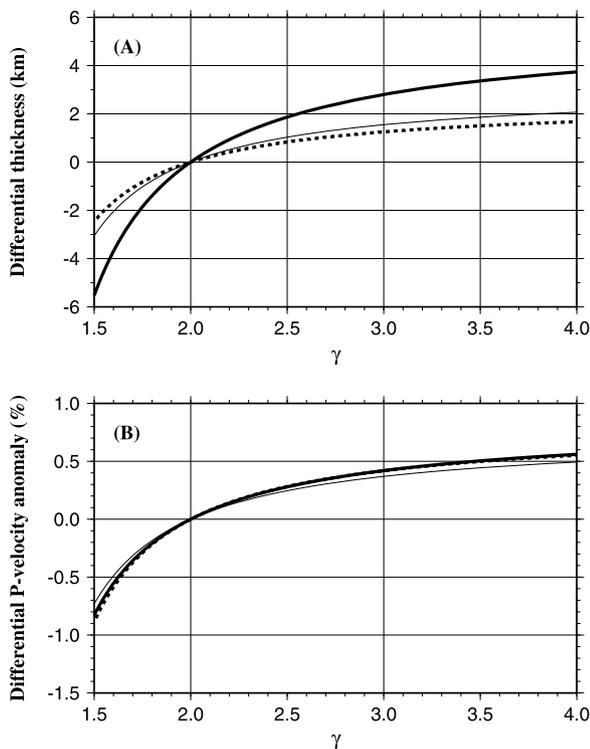
Fig. 8. (A) Variations of the depth to the d410 (solid thin line) and d660 (solid thick line) and MTZ thickness (dashed line) as a function of γ where $\gamma = (\delta V_s/V_{s0})/(\delta V_p/V_{p0})$. (B) Variations of P-wave velocity anomalies above the d410 (solid thin line) and the d660 (solid thick line) and that in the MTZ (dashed line). For both plots the values are relative to those when $\gamma = 2.0$.

Expecting constant depth and velocities in such a large area is certainly unrealistic.

Fortunately, the large number of RFs needed in order to enhance the Pds and Ppds phases usually come from events with vastly different back-azimuths and epicentral distances and thus the rays travel through or reflect at the discontinuity at different locations (see Fig. 2 for the spatial distribution of the Ppds ray-piercing points at the center of the MTZ for Area C). When the RFs are stacked, random undulations in the depth of the discontinuity are smoothed out, and the results are spatially-averaged (weighted by ray-density). If the undulations are not random but the discontinuity possesses a regional tilt, the resulting discontinuity depth is azimuthally dependent and when all the RFs from different azimuths are used, the resulting pulses on the Pds and Ppds curves (Fig. 3) are significantly broadened or have multiple peaks. The fact that all the arrivals associated with the d410 and d660 for the areas (Figs. 3 and 6) are clear and sharp suggests that there is no significant regional tilting of the discontinuities in the area sampled by the rays. Caution should be exercised for areas with anticipated large variations in MTZ discontinuity depth and with non-random lateral variations of seismic velocities in the upper mantle and the mantle transition zone. In addition, a large (e.g., 2500 or greater) number of high-quality RFs recorded by stations in a sizable (e.g., radius $\geqslant 1.5°$) area are needed in order to obtain reliable results.

7. Conclusions

Relative to techniques that utilize only the Pds phase, the procedure described here has the potential to delineate more realistic spatial variations of the depth to the discontinuities and MTZ thickness, by minimizing the trade-offs between the discontinuity depth and velocity anomalies in the overlying layers. The re-

fined spatial variations, when combined with the simultaneously determined velocity anomalies, provide important constraints on the in-situ temperature in the vicinity of the MTZ discontinuities, which are essential for addressing such long-standing controversies as upper, middle, or lower mantle origin of mantle plumes and the fate of subducted slabs. They also shed lights on the existence and thickness of proposed water-rich layers above the MTZ discontinuities. The approach can also be used to image possible discontinuities in the upper mantle, which are usually masked by multiply reflected/converted phases associated with the Moho and the free surface when only the Pds phases are used. Therefore, this approach, when applied to data from USArray-type high-quality, high-density data sets, should provide refined constraints on the layered structure and physical and chemical properties in the Earth's deep interior.

Acknowledgements

Appendix A. Supplementary material

Supplementary material related to this article can be found online at http://dx.doi.org/10.1016/j.epsl.2013.08.025.

References

Ai, Y., Zhao, D., Gao, X., Xu, W., 2005. The crust and upper mantle discontinuity structure beneath Alaska inferred from receiver functions. Phys. Earth Planet. Inter. 150, 339–350. http://dx.doi.org/10.1016/j.pepi.2004.12.002.

Ammon, C.J., 1991. The isolation of receiver effects from teleseismic *P*-wave-forms. Bull. Seismol. Soc. Am. 81, 2504–2510.

Andrews, J., Deuss, A., 2008. Detailed nature of the 660 km region of the mantle from global receiver function data. J. Geophys. Res. 113, B06304. http://dx.doi.org/10.1029/2007JB005111.

Bina, C.R., Helffrich, G., 1994. Phase transition Clapeyron slopes and transition zone seismic discontinuity topography. J. Geophys. Res. 99, 15,853–15,860.

Cao, A., Levander, A., 2010. High-resolution transition zone structures of the Gorda Slab beneath the western United States: Implication for deep water subduction. J. Geophys. Res. 115, B07301. http://dx.doi.org/10.1029/2009JB006876.

Clarke, T.J., Silver, P.G., 1991. A procedure for the systematic interpretation of body wave seismograms I. Application to Moho depth and crustal properties. Geophys. J. Int. 104, 41–72.

Cornwell, D.G., Hetenyi, G., Blanchard, T.D., 2011. Mantle transition zone variations beneath the Ethiopian Rift and Afar: Chemical heterogeneity within a hot mantle? Geophys. Res. Lett. 38 (16). http://dx.doi.org/10.1029/2011GL047575.

Das-Sharma, S., Ramesh, D.S., Li, X., Yuan, X., Sreenivas, B., Kind, R., 2010. Response of mantle transition zone thickness to plume buoyancy flux. Geophys. J. Int. 180, 49–58. http://dx.doi.org/10.1111/j.1365-246X.2009.04403.x.

Dueker, K.G., Sheehan, A.F., 1997. Mantle discontinuity structure from midpoint stacks of converted P to S waves across the Yellowstone hotspot track. J. Geophys. Res. 102, 8313–8327.

Efron, B., Tibshirani, R., 1986. Bootstrap methods for standard errors, confidence intervals, and other measures of statistical accuracy. Stat. Sci. 1, 54–75.

Fee, D., Dueker, K., 2004. Mantle transition zone topography and structure beneath the Yellowstone hotspot. Geophys. Res. Lett. 31, L18603. http://dx.doi.org/10.1029/2004GL020636.

Flanagan, M.P., Shearer, P.M., 1998. Global mapping of topography on transition zone velocity discontinuities by stacking SS precursors. J. Geophys. Res. 103, 2673–2692.

Fouch, M.J., 2012. The Yellowstone hotspot: Plume or not? Geology 40, 479–480. http://dx.doi.org/10.1130/focus052012.1.

Foulger, G.R., Pritchard, M.J., Julian, B.R., Evans, J.R., Allen, R.M., Nolet, G., Morgan, W.J., Bergsson, B.H., Erlendsson, P., Jakobsdottir, S., Ragnarsson, S., Stefansson, R., Vogfjord, K., 2001. Seismic tomography shows that upwelling beneath Iceland is confined to the upper mantle. Geophys. J. Int. 146, 504–530.

Gao, S.S., Silver, P.G., Liu, K.H., the Kaapvaal Seismic Group, 2002. Mantle discontinuities beneath Southern Africa. Geophys. Res. Lett. 29 (10), 1291–1294. http://dx.doi.org/10.1029/2001GL013834.

Gao, S.S., Liu, K.H., in preparation. Spatial variation of mantle transition zone discontinuities beneath the western and central United States using multiply-reflected P-to-S conversions.

Gu, Y., Dziewonski, A.M., Agee, C.B., 1998. Global de-correlation of the topography of transition zone discontinuities. Earth Planet. Sci. Lett. 157, 57–67.

Gurrola, H., Minster, J.B., Owens, T., 1994. The use of velocity spectrum for stacking receiver functions and imaging upper mantle discontinuities. Geophys. J. Int. 117 (2), 427–440.

Jasbinsek, J.J., Dueker, K.G., Hansen, S.M., 2010. Characterizing the 410 km discontinuity low-velocity layer beneath the LA RISTRA array in the North American Southwest. Geochem. Geophys. Geosyst. 11, Q03008. http://dx.doi.org/10.1029/2009GC002836.

Karato, S., 1993. Importance of anelasticity in the interpretation of seismic tomography. Geophys. Res. Lett. 20, 1623–1626. http://dx.doi.org/10.1029/93GL01767.

Kennett, B.L.N., Engdahl, E.R., 1991. Traveltimes for global earthquake location and phase identification. Geophys. J. Int. 105, 429–465.

Lawrence, J.F., Shearer, P.M., 2006. A global study of transition zone thickness using receiver functions. J. Geophys. Res. 111, B06307. http://dx.doi.org/10.1029/2005JB003973.

Leeman, W.P., Schutt, D.L., Hughes, S.S., 2009. Thermal structure beneath the Snake River Plain: Implications for the Yellowstone hotspot. J. Volcanol. Geotherm. Res. 188, 57–67. http://dx.doi.org/10.1016/j.jvolgeores.2009.01.034.

Li, A., Fischer, K.M., Wysession, M.E., Clarke, T.J., 1998. Mantle discontinuities and temperature under the North American continental keel. Nature 395, 160–163.

Liu, K.H., 2003. Effects of inelasticity on the apparent depth and detectability of seismic discontinuities in the mantle. Geophys. Res. Lett. 30 (9), 1455. http://dx.doi.org/10.1029/2002GL015264.

Liu, K.H., Gao, S.S., 2006. Mantle transition zone discontinuities beneath the Baikal rift and adjacent areas. J. Geophys. Res. 111, B11301. http://dx.doi.org/10.1029/2005JB004099.

Liu, K.H., Gao, S.S., 2010. Spatial variations of crustal characteristics beneath the Hoggar swell, Algeria revealed by systematic analyses of receiver functions from a single seismic station. Geochem. Geophys. Geosyst. 11, Q08011. http://dx.doi.org/10.1029/2010GC003091.

Liu, K.H., Gao, S.S., Silver, P.G., Zhang, Y., 2003. Mantle layering across central South America. J. Geophys. Res. 108 (B11), 2510. http://dx.doi.org/10.1029/2002JB002208.

Obrebski, M., Allen, R.M., Pollitz, F., Hung, S.-H., 2011. Lithosphere–asthenosphere interaction beneath the western United States from the joint inversion of body-wave traveltimes and surface-wave phase velocities. Geophys. J. Int. 185, 1003–1021. http://dx.doi.org/10.1111/j.1365-246X.2011.04990.x.

Ohtani, E., Litasov, K.D., 2006. The effect of water on mantle phase transitions. Rev. Mineral. Geochem. 62, 397–420. http://dx.doi.org/10.2138/rmg.2006.62.17.

Ozacar, A.A., Gilbert, H., Zandt, G., 2008. Upper mantle discontinuity structure beneath East Anatolian Plateau (Turkey) from receiver functions. Earth Planet. Sci. Lett. 269, 427–435. http://dx.doi.org/10.1016/j.epsl.2008.02.036.

Ringwood, A.E., 1975. Composition and Petrology of the Earth's Mantle. McGraw–Hill, New York.

Schaeffer, A.J., Bostock, M.G., 2010. A low-velocity zone atop the transition zone in northwestern Canada. J. Geophys. Res. 115, B06302. http://dx.doi.org/10.1029/2009JB006856.

Schmandt, B., Humphreys, E., 2010. Seismic heterogeneity and small-scale convection in the southern California upper mantle. Geochem. Geophys. Geosyst. 11, Q05004. http://dx.doi.org/10.1029/2010GC003042.

Schmandt, B., Dueker, K., Humphreys, E., 2012. Hot mantle upwelling across the 660 beneath Yellowstone. Earth Planet. Sci. Lett. 331–332, 224–236. http://dx.doi.org/10.1016/epsl.2012.03.025.

Shearer, P.M., 1991. Constraints on upper mantle discontinuities from observations of long-period reflected and converted phases. J. Geophys. Res. 96 (B11), 18,147–18,182.

Shearer, P.M., 2000. Upper mantle seismic discontinuities. In: Karato, S., et al. (Eds.), Earth's Deep Interior.

Shen, Y., Solomon, S.C., Bjarnason, I.T., Wolfe, C.J., 1998. Seismic evidence for a lower-mantle origin of the Iceland plume. Nature 395, 62–65.

Sheriff, R.E., Geldart, L.P., 1993. Exploration Seismology, second ed. Cambridge Univ. Press, New York.